ELSEVIER

A new protocol for characterization of dislocations in photovoltaic polycrystalline silicon solar cells

Karem Boubaker

Photovoltaic and Semiconductor Materials Laboratory, E.N.I.T. TUNISIA/63 Rue Sidi Jabeur, 5100 Mahdia, Tunisia

Abstract

Main photovoltaic properties of polycrystalline silicon solar cells are often affected by dislocation effects. Dislocations degrade functional photocurrent and considerably alter relevant parameters such as short-circuit current density, dark current intensity and open-circuit voltage. In this study, we have developed an enhanced photothermal technical protocol for diagnosing dislocation spatial distribution inside photovoltaic polycrystalline silicon solar cells. We tried to establish a qualitative and quantitative correlation between the local thermal properties alteration and dislocation spatial range. Experimental imaging profiles, yielded by this technique are compared to other diagnostic techniques results.

1. Introduction

Photovoltaic polycrystalline silicon solar cells provide a clean and renewable source of energy. Such devices operate by absorbing light and using the discrete energy from the received photons to pump electrons to their excited state. The excited electrons migrate through the material's layers and produce an electrical current. The silicon crystal absorbs the light and the excited electrons then hop to the edge layer. The electrons are then transferred as an electrical current, through appropriate materials such as carbon or as metallic film. A current is produced by this process and can be recuperated and used in an external device. Advances [1–4] in multicrystalline silicon technology have stimulated photovoltaic device manufacturing activities. Nowadays, a simple prototype cell can be produced by block-casting or ribbon techniques, ensuring both efficiency requirements and low-cost production. However, as multicrystalline silicon structure is inhomogeneous, and many efforts have been performed in order to track defects recombination activities, partially due to this inhomogeneity, like dislocations and grain boundaries. Dislocations are commonly defined as the intrinsic extended defects inside the polycrystalline silicon structure. They generally act as recombination centers that decrease the minority lifetime and performance of photovoltaic sensitive elements. Several recent studies [4,12,20,21] have demonstrated that these dislocations exert a considerable effect on photovoltaic active parts and also affect relevant parameters such as short-circuit current density, dark current intensity or open circuit voltage. Since the recombination intensities are strongly influenced by the presence of transition metals, it is important to know how to eliminate their spatial distribution and monitor their material behavior according to this distribution. Such knowledge undoubtedly provides a guideline for investigating these material interactions with impurities inside the polycrystalline silicon solar cells, and comparing them with differently contaminated silicon device. In this paper, we try to characterize such dislocations in a contaminated photovoltaic solar cell using enhanced 'Mirage Effect' technique.

2. Dislocation imaging techniques

In this part, some of most up-to-dated imaging techniques are described [1–7], in order to introduce the

E-mail address: boubaker_karem@yahoo.com

Nomenclature

b	Gaussian beam radius (m)	Q_C	convective heat per unit volume ($W\,m^{-2}$)
D	thermal diffusivity ($m^2\,s^{-1}$)	Q_r	radiative heat per unit volume ($m^2\,s^{-1}$)
f	chopper (modulation) frequency (Hz)	T	absolute temperature (K)
h	convection transfer coefficient ($W\,m^{-2}\,K^{-1}$)	z_0	probe beam offset (m)
k	thermal conductivity (Hz)	λ	thermal wavelength (m)
P	light source power (W)	ψ	photothermal deflection (rad)
Q	deposited pumped heat ($W\,m^{-3}$)	ω	pulsation ($rad\,s^{-1}$)
		Φ	energy flow ($W\,m^{-2}$)
		σ_0	Stephan–Boltzman constant ($W\,m^{-2}\,K^{-4}$)

actual proposed method and show its advantages. Performance description is restricted to dislocation localization skill since the imaging research field is much more extended.

2.1. Transmission electron microscopy

Transmission electron microscopy consists of bombarding a thin wafer sample by a highly focused beam of monoenergetic electrons (Fig. 1). An acceleration potential (300–500 kV) produces a highly focused flow of coherent and synchronous electrons with a small wavelength (about 2.2 pm). The electrons drop normally to the targeted surface. This feature ensures high point-to-point resolution and high electron mean free path for greater penetration depth. The beam has enough energy for the electrons to be transmitted through the wafer.

2.2. Scanning defect mapping technique

Scanning defect mapping technique uses optical scattering to map dislocations distribution in silicon semiconductor wafers. First, a wafer is treated with a developed etch of acids (hydrofluoric, acetic) in order to amplify the light scattered by the defects. During exposure, each etch produces V-shaped grooves at the grain boundaries and circular or elliptical pits at the dislocations. The grooves produced at the grain boundaries scatter light in a streak-like shape perpendicular to the length of the grain boundary. Scanning is ensured by moving a treated wafer across a stationary laser beam and mapping the defects at each location on the wafer. Citarella et al. [12] used a similar technique by measuring microwaves photoconductivity inside semiconductor device.

2.3. Noise equivalent temperature difference (NETD) technique

Noise equivalent temperature difference is a recent dislocation imaging technique developed by Haakenaasen [13] and earlier by Goodberlet [14]. This technique is applied to $Cd_xHg_{1-x}Te$ layers grown by molecular beam epitaxy. The authors noticed that the grown layers had varying densities of needle-shaped structures on the surface; they submitted the targeted surface to a micrometrical indirect scanning using a set of mid-wavelength infrared sensitive diodes (MWIR-D).

The set-up of this technique is presented in Fig. 2a with, as a main part, a photodiode camera. The sensitive part of this camera contains a 64×64 element 2D array of
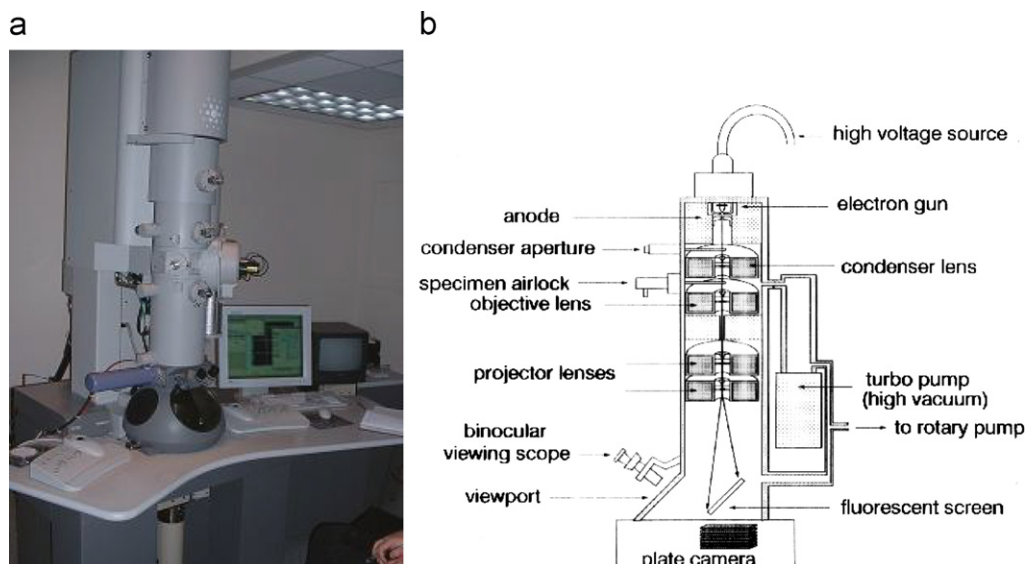

Fig. 1. Transmission electron microscopy set-up.
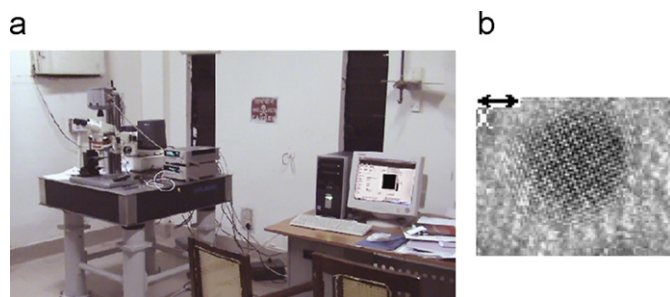
Fig. 2. Noise equivalent temperature difference (NETD) technique: (a) MWIR-D set-up and (b) an imaging sample.

$16 \times 16\,\mu m^2$ MWIR diodes, which are hybridized to read-out electronics and give median NETD of 60 mK. A micrometrical image from a 2D array is shown in Fig. 2b.

2.4. Large-scale amplified laser scanner technique

The large-scale laser scanner technique is widely used to identify the dislocation and alteration of performance within photovoltaic cells, submodules, and modules. It consists on a central computer-controlled system that scans a laser beam across a photovoltaic device, then amplifies and records the resulting laser-beam-induced current as a function of the laser position. The results are presented as a one-coordinate modulated map, a line scan, or as a color-coded map. This technique, like the imaging techniques used by H.J. Lewerenz, Macht et al. [15], uses narrow range lasers with wavelength between 488 and 633 nm, which is characteristic of a large part of the solar spectrum.

3. Enhanced 'mirage effect' technique

3.1. Technique principle

3.1.1. Mirage effect phenomena and its applications in physics

When a targeted sample receives an incident heat from a source, it acts subsequently, and under some conditions, as a secondary source that heats ambient fluid. Heat flow that moves from the heated surface to the fluid induces a temperature gradient associated to a gradient of the medium refraction index. Common terminology of 'mirage' term does not distance from this phenomenon. In fact the desert-misled hallucinations are obviously not only psychological. Heat reflected toward hot air causes its refraction index to vary so that it could become equal to water or any other liquid index. Under such circumstances vision could be led to error. In physical search, this phenomenon is incorporated in several applications. Heat source are generally electrical or light supplies. Ambient fluid is usually air, a defined gas or a transparent liquid (paraffin, CCl_4). Most known techniques differ according to the means of both index detection and source modulation. For example, the pulse techniques focus on fluid time-response to a unit-level

excitation while the frequencal techniques are based on recording response to continuously modulated heat. The actually used 'mirage effect' technique is conventionally considered as a frequencal protocol. This technique details are developed in many studies [6,7,18].

3.1.2. Photothermal signal detection (PSD)

'Mirage effect' technique consists of measuring the temperature or the refraction index variations in the ambient fluid, while the targeted surface is heated. As verified experimentally, the temperature variations are quick and sometimes too small; the recourse to thermometers or thermocouples is not suitable. Among the well-known alternative measurement devices, probe beam deflection (PBD) setting is the most adopted. The main part of PBD settings is a laser beam that runs over the prospected area with a prefixed disposition beside targeted surface (offset) and geometrical relative position (parallel or normal to targeted surface). In the case of a modulated heat (pumped at a preset frequency), the probe beam is deviated at the same frequency but not necessary with the same phase and amplitude. The PSD is hence a set of measurements that leads to the determination of the probe beam response parameters.

3.1.3. Dislocation mapping

The homogenous material response to Mirage Effect solicitation is supposed to be uniform. When irregularities are unveiled by photothermal imaging, they can be classified with reference to standard defects. In fact, the previous scanning of artificially provoked similar defects, yields classifiable records [8,9] of the photothermal response parameters (amplitude, phase-shift, frequency). For example, dislocations in silicon semiconductor wafers cause photothermal signal phase rise in a defined way while amplitude is attenuated to 50%.

3.2. Technique experimental set-up

3.2.1. Synoptic scheme

The 'mirage effect' set-up is wholly presented in Fig. 3. The targeted sample is fixed to a Plexiglas sink mounted on a sliding platform. Platform-sample displacement unit is a digital pulse-signal generator that monitors two axis positions through two micrometrical DC motors. This disposal is more widely described in precedent works [6–9].

3.2.2. Heat source modulated beam

The heat source (Fig. 4) is a common photo-electrical laser diode (power $P = 0.1$ W, wavelength $\lambda_s = 6.70 \times 10^{-7}$ m) coupled to a flexible optic fiber [6–8]. The use of optic fiber permits the independent spatial set-up of the heat source and the sample sides. The modulation of heat source is the duty of a mechanical chopper. The transmitted heat is chopped at a pre-set frequency f (between 2 and 500 Hz). The mechanical modulator main part is a pierced wheel located between the optic fiber free extremity and the
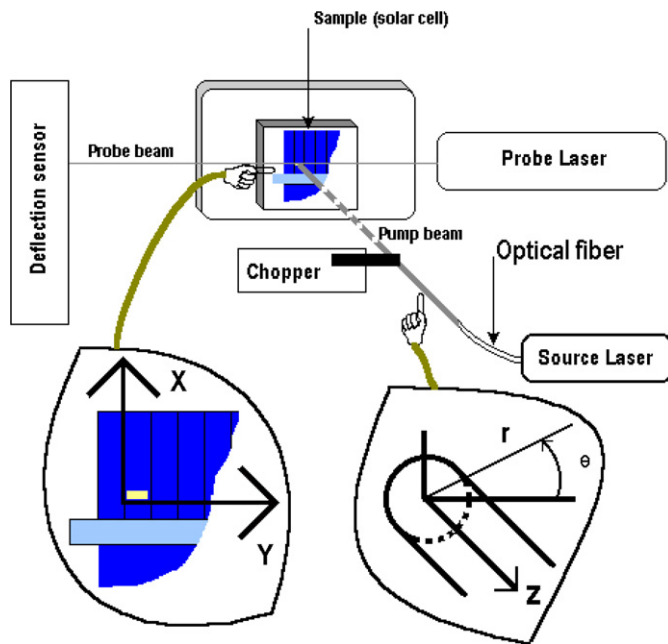
Fig. 3. 'Mirage effect' set-up synoptic scheme.

Fig. 4. Pump laser beam settings.

3.2.3. Probe beam and synchronous detection unit (SDU)

The probe beam is provided by a weak laser diode ($P = 1.0 \times 10^{-3}\,\mathrm{W}$, $\lambda_{\mathrm{p}} = 6.33 \times 10^{-7}\,\mathrm{m}$). The beam path is smoothened by interposing two convergent lens appropriately distanced from the source targeted area. The probe beam offset is fixed, at each experimental sequence beginning, thanks to two endless micrometrical screws bolted to the sample-sink sliding platform [2,3,10]. The probe beam path crosses pump beam perpendicularly (Fig. 5), then it hits a photodiode cell, coupled to a SDU. As the mechanical chopper rates the energy flow to targeted surface, the photothermal deflection occurs simultaneously and at the same frequency f. Nevertheless, noise and uncontrolled harmonics can interfere with the signal and induce an error [10]. The synchronous deflection detector (Fig. 6) avoids recording such perturbations since it is adjusted to detect exclusively the signal with same chopper frequency, the way that variations can be securely attributed to the source effect. An internal synchronous
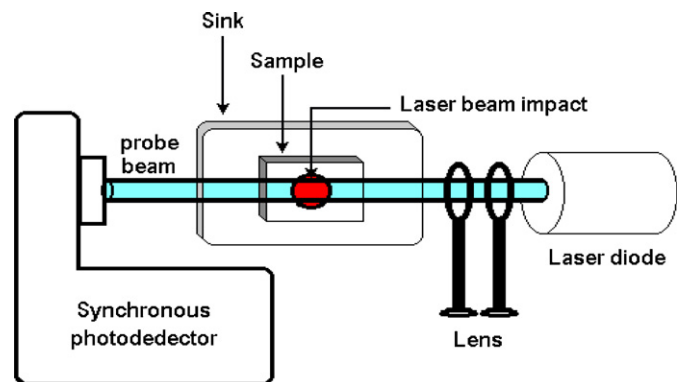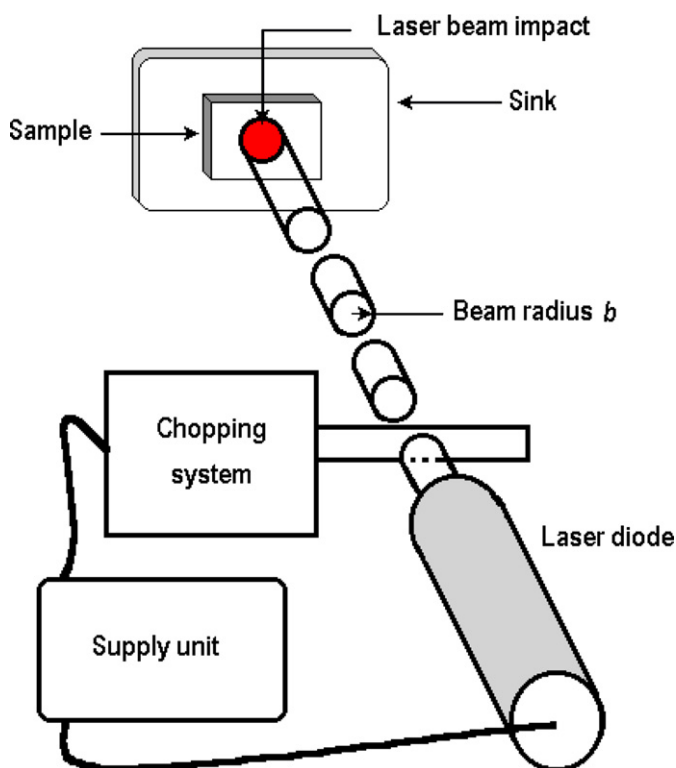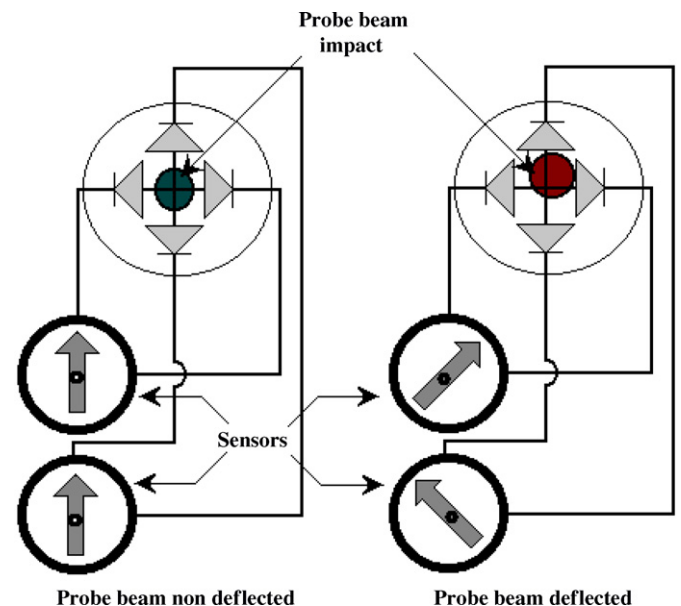

Fig. 5. Probe laser beam settings.

Fig. 6. Photodiodes synchronous deflection detector.

targeted sample surface [8–10]. The wheel speed is controlled by an accurate feed-back DC motor. The photo-electrical laser diode emitted beam radius is controlled by an optical micrometrical diaphragm mounted on the optic fiber free extremity.

trigger, connected to the central unit, eliminates any harmonic component with frequency out from a narrow band centered on chopper frequency.

4. Analytical derivation of temperature and photothermal signal expressions

In this part, a solution to main heat equation is proposed.

4.1. Temperature expression

It is known that when a body is heated by a distant source, and when a determined fluid separates source from target, incident energy flow induces, inside the bulk fluid, a temperature gradient expressed by

$$\vec{\phi} = -k \times \overrightarrow{\text{grad}}(T), \tag{1}$$

where k is the thermal conductivity (in $\text{W m}^{-1}\text{K}^{-1}$) and T is the absolute temperature (in K).

In the case of a modulated Gaussian beam, the heat energy transmitted from the target to the fluid per unit volume, and at a pulse frequency f is expressed by

$$Q(r,t) = Q = Q_0\, e^{-2(r^2/b^2)}\, e^{-j\omega t}, \tag{2}$$

where Q_0 is the nominal heat transmitted from the target to the bulk fluid elementary volume, whose value depends on both fluid and targeted surface thermal parameters, $\omega = 2\pi f$, and b is the Gaussian beam external radius. Taking in account conductive, radiative and convective [7–10] heat from target to fluid, Eq. (1) becomes

$$\nabla^2 T - \frac{1}{D_g}\frac{\partial T}{\partial t} = -\frac{Q + Q_C + Q_r}{k}, \tag{3}$$

where

$$Q_C = \pi h T_0 b^2 [e^{(z_0/\lambda_g)} - 1],$$

$$Q_r = \frac{\sigma_0 \sqrt{\pi}(T_0^4 - T_\infty^4)}{4b}$$

with Q, source term given by Eq. (1) (in W m^{-3}); Q_C, convective heat transferred per unit volume (in W m^{-3}); Q_r, radiative heat transferred per unit volume (W m^{-3}); D_g, fluid medium thermal diffusivity (in m^2s^{-1}); λ_g, defined by $\lambda_g^2 = j\omega/D_g$; k, fluid thermal conductivity (in $\text{W m}^{-1}\text{K}^{-1}$); σ_0, Stephan–Boltzman constant (in $\text{W m}^{-2}\text{K}^{-4}$); z_0, probe beam offset above targeted surface (in m); h, global convection heat transfer coefficient of the process (in $\text{W m}^{-2}\text{K}^{-1}$); T_0, maximum central absolute temperature (in K); T_∞, room mean absolute temperature (in K); and b, radius of the Gaussian beam (in m).

The solution to Eq. (3), expressed in cylindrical coordinates is proposed in other studies [6–10,18,19] as expression (4):

$$T(r,z) = \sum_{m=1}^{+\infty} \eta_m J_0\left(X_m \times \frac{r}{b}\right) e^{-(z/\lambda_g)}, \tag{4}$$

where X_m is mth root of $J_0(x)$ polynom. The solution is thus an infinite sum of elementary solutions pondered by the coefficients η_m. These coefficients are solutions of the quasi-infinite order system

$$\begin{cases} \dfrac{d\left[\sum_{m=1}^{+\infty} \eta_m \left\langle \xi_m^2 J_0''(\xi_m r) + (\xi_m/r) J_0'(\xi_m r) + J_0(\xi_m r)\right\rangle\right]}{dr} = 0, \\ \xi_m = \dfrac{X_m}{b} \quad \text{with } X_m\ m\text{th root of } J_0(x) \quad r \in [0;b]. \end{cases} \tag{5}$$

The determination of the coefficients values was achieved by choosing a pre-set number N of coefficients η_m to determine, and effectuating an N-order sampling inside the interval [0; b]. System (5) yields thus a simple N^2-system, solved by appropriate array process methods (Cholesky, Householder [10,11]).

4.2. Photothermal signal parameters

The probe beam deflection ψ is thus calculated, in the case of a non-uniform heating [7] through expression (6) of its normal and radial respective components ψ_z and ψ_r:

$$(\psi) = \begin{pmatrix} \psi_z \\ \psi_r \end{pmatrix} = \begin{pmatrix} \frac{1}{T_0}\int_0^{+\infty} \frac{\partial T}{\partial z} \\ \frac{1}{T_0}\int_0^{+\infty} \frac{\partial T}{\partial r} \cos\theta \end{pmatrix} \tag{6}$$

with T expression obtained through the solution of system (5). The theoretical calculations based on Eqs. (4) and (5) yielded for a small offset z_0, expression (7) of ψ_z and ψ_r as complex values

$$(\psi) = \begin{pmatrix} \psi_z \\ \psi_r \end{pmatrix} = \begin{pmatrix} |\psi_z|\, e^{-j(\omega t - \phi_z)} \\ |\psi_r|\, e^{-j(\omega t - \phi_r)} \end{pmatrix}. \tag{7}$$

The calculus of $|\psi_z|$, $|\psi_r|$, ϕ_z and ϕ_r which are photothermal signal radial and normal components amplitudes and phases, is detailed in precedent studies [2,6,10].

5. Experiment

5.1. Sample description

The studied sample is a photovoltaic polycrystalline silicon solar cell wafer taken from AEG PQ40 PV 12-year-old module (Fig. 7a and b). The prospected zone is a small 3.0×12.0 mm rectangle situated at 2.0 mm from a conduction bar (Fig. 7a).

5.2. Measurement and results

The measurements consist of a simultaneous detection of the photothermal deflection signal both phase ϕ_z and amplitude $|\varphi_z|$ perturbations for several targeted points by scanning the sample surface vicinity. Different offset values (distance between probe beam lower edge and targeted surface, which is relevant for determining the dislocations depth) are fixed by micrometrical screws. The beam radius b value is 0.40 mm, modulation frequency f is 47.0 Hz, under these circumstances, the thermal wavelengths are
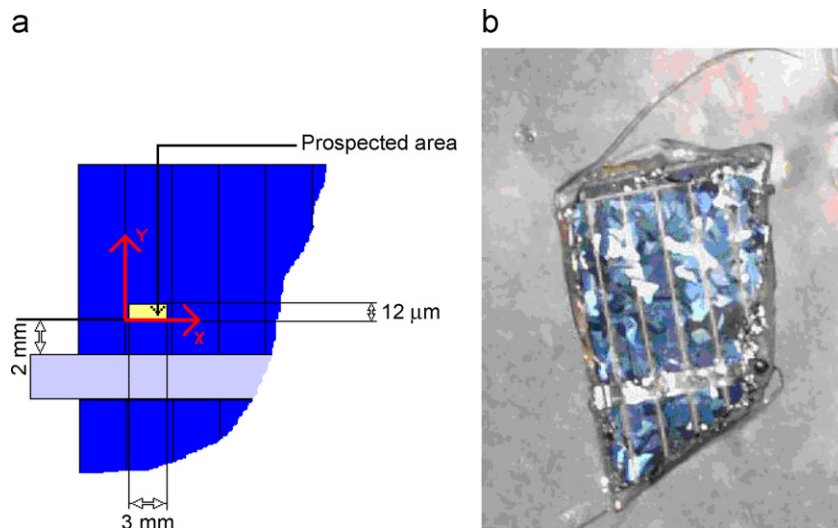
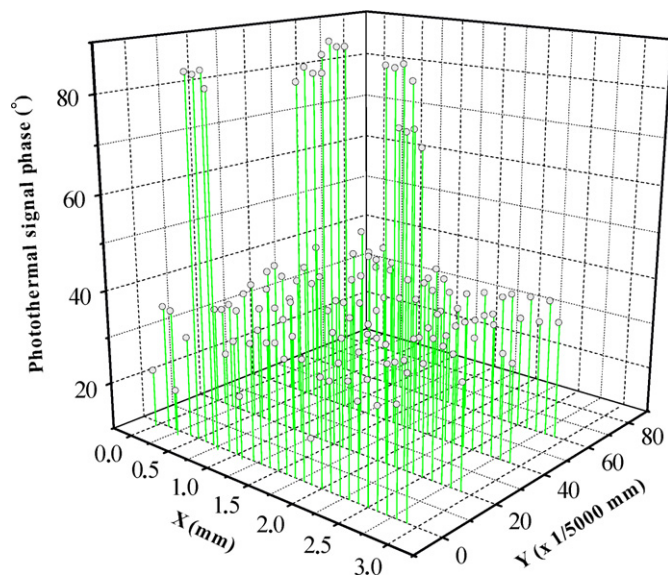Fig. 7. (a) Studied sample (geometry) and (b) studied sample (photography).

Fig. 8. Sample photothermal signal phase imaging. (Targeted surface is mapped in X–Y plane. Photothermal signal phase is measured for each position.)

Fig. 9. Comparison between TEM and photothermal imaging. (Photothermal picture is projected on X–Y plane as an upper view.)

0.17 mm in solid sample and 0.24 mm in fluid [10]. Photothermal signal phase imaging is then performed using the scanned values (Fig. 8).

5.3. Result analysis

The yielded photothermal signal phase profile shows important phase-shift irregularities at values of X-coordinate: $0.5\,\text{mm} < X < 0.9\,\text{mm}$. These irregularities consist of a phase shift rise from $32°$ to $83°$ which occurs for several distant values of Y-coordinate, respectively: 0.0, 8.2×10^{-3} and 15.4×10^{-3} mm. As the irregularities locations seem to stay parallel to the straight line ($X = 0$), which corresponds to conduction ribbon lines edge. This zone area is analyzed
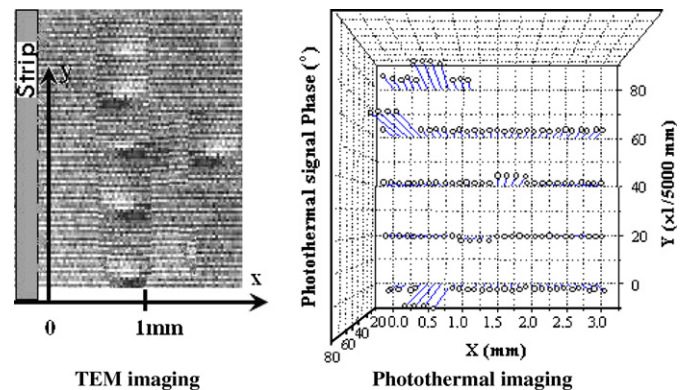
whit TEM imaging, displayed conjointly with actual profile (Fig. 9), and identified as a dislocations-rich area. An additional imaging at outer area yielded a quasi-constant photothermal signal phase ($\approx 32.0°$), feature that confirms upper analysis. The comparison with other techniques analysis results yielded by our laboratory colleagues [16,17] confirms our results.

6. Conclusion

Nowadays, photothermal signal imaging (PSI) technique, as a defect characterization tool in photovoltaic device technology, is of increasing importance [1–6]. This work presents a supply to recent works on dislocation monitoring inside the newly proposed and implemented photovoltaic cells material. 'mirage effect' technique can give a reliable diagnostic and an accurate image mapping as a contribution to actually performed techniques, like transmission electron microscopy (TEM), photoluminescence spectroscopy (PS) and laser scanner technique (LCT) [1,4,12,15].

The proposed technique is mainly non-destructive, clean and quick. It gives also a possibility of cataloguing other main defects as cracks or bubbles according to the thermal response, which is easy to measure. We are now focusing on studying the dislocations photothermal response inside the photovoltaic polycrystalline silicon cells being under light or electrical load.

References

[1] S. Ostapenko, I. Tarasov, J.P. Kalejs, Semicond. Sci. Technol. 15 (2000) 840.

[2] K. Boubaker, M. Bouhafs, N. Yacoubi, J. Non-Destr. Test. Eval. 36 (8) (2003) 547.

[3] K. Boubaker, Journal du 1er Congrès Maghrébin de Génie Électrique, Tunis.' C.M.G.E'94, vol. 1, pp. MC51–MC53.

[4] H. El Ghitani, M. Pasquinelli, S. Martinuzzi, J. Phys. III, France 3 (1993) 1941.

[5] F. Lepoutre, D. Fournier, A.C. Boccara, Non-destructive Characteristic of Materials II, Plenium Pub. Corporation, 1987.

[6] K. Boubaker, Eur. Phys. J. Appl. Phys. (2004) 15525.

[7] K. Boubaker, Int. J. Heat Technol. 20 (2002) 31.

[8] K. Boubaker, Thèse de Doctorat, Université de Tunis-Elmanar, TUNISIE, 27-Février, 2003.

[9] N. Yacoubi, B. Girault, J. Fesquet, Appl. Opt. IV 25 (1999) 4622.

[10] K. Boubaker, IEEE Proceedings, Journal of First International Symposium on Control, Communications and Signal Processing ISCCSP 2004, IEEE catalog number 04EX814, ISBN 0-7803-8379-6, Hammamet, Tunisia, pp. 877–880.

[11] L.C. Aamodt, J.C. Murphy, J. Phys. IV 4 (1994) C7.

[12] G. Citarella, S. von Aichberger, M. Kunst, Mater. Sci. Eng. B 91–92 (2002) 124.

[13] R. Haakenaasen, Phys. Scripta T126 (2006) 31.

[14] M.A. Goodberlet, IEEE Trans. Geosci. Remote Sens. 38 (2000) 1362.

[15] B. Macht, M. Turrión, A. Barkschat, P. Salvador, K. Ellmer, H. Tributsch, Sol. Energy Mater. Sol. Cells 730 (2002) 163.

[16] R. Brini, M. Kanzari, B. Rezig, J. Werckmann, Eur. Phys. J. Appl. Phys. 30 (2005) 153.

[17] A. Bouzidi, A.S. Bouazzi, B. Rezig, Eur. Phys. J. Appl. Phys. 31 (2005) 11.

[18] I. Mellouki, O. Touayar, T. Ktari, F. Saadallah, J. Bastie, N. Yacoubi, Meas. Sci. Technol. 15 (2004) 384.

[19] F. Durand, Sol. Energy Mater. Sol. Cells 72 (2002) 125.

[20] T. Kieliba, S. Riepe, W. Warta, J. Appl. Phys. 100 (2006) 063706.

[21] P.J. Cousins, J.E. Cotter, in: Photovoltaic Specialists Conference, Conference Record of the Thirty-First IEEE, 2005, pp. 1047–1050.